# Chitosan-based GOx@Co-MOF composite hydrogel: A promising strategy for enhanced antibacterial and wound healing effects

Fangyu Liu, Jie Song, Sihan Li, Haozhi Sun, Jinjun Wang, Feng Su, Suming Li, S.M. Li

# Chitosan-Based GOx@Co-MOF Composite Hydrogel: A Promising Strategy for Enhanced Antibacterial and Wound Healing Effects

Fangyu Liu,[a,b] Jie Song,[a,b], Sihan Li, [a,b] Haozhi Sun, [a,b] Jinjun Wang,[c]* Feng Su,[a,b] * Suming Li [d] *

[a] *State Key Laboratory Base of Eco-chemical Engineering, College of Chemical Engineering, Qingdao University of Science and Technology, Qingdao 266042, China*

[b] *Institute of High Performance Polymers, Qingdao University of Science and Technology, Qingdao 266042, China*

[c] *Qingdao Traditional Chinese Medicine Hospital (Qingdao Hiser Hospital), Qingdao 266033, China*

[d] *Institut Europeen des Membranes, UMR CNRS 5635, Universite de Montpellier, 34095 Montpellier, France*

*Corresponding authors: yayang2001@163.com (J. Wang); sufeng@qust.edu.cn (F. Su); suming.li@umontpellier.fr (S. Li)



## Abstract

A novel composite hydrogel was synthesized via Schiff base reaction between chitosan and di-functional poly(ethylene glycol) (DF-PEG), incorporating glucose oxidase (GOx) and cobalt metal-organic frameworks (Co-MOF). The resulting CS/PEG/GOx@Co-MOF composite hydrogel was characterized using Fourier transform infrared spectroscopy (FTIR), scanning electron microscopy (SEM), X-ray photoelectron spectroscopy (XPS), thermogravimetric analysis (TGA), and energy-dispersive X-ray spectroscopy (EDS). The results confirmed successful integration and uniform

distribution of Co-MOF within the hydrogel matrix. Functionally, the hydrogel exploits the catalytic decomposition of glucose by GOx to generate gluconic acid and hydrogen peroxide ($H_2O_2$), while Co-MOF gradually releases metal ions and protects GOx. This synergy enhanced the antibacterial activity of the composite hydrogel against both Gram-positive (*S. aureus*) and Gram-negative bacteria (*E. coli*), outperforming conventional chitosan-based hydrogels. The potential of the composite hydrogel in treating wound infections was evaluated through antibacterial and wound healing experiments. Overall, CS/PEG/GOx@Co-MOF hydrogel holds great promise for the treatment of wound infections, paving the way for further research and potential clinical applications.

**Keywords:** Metal-organic framework; Chitosan; Poly(ethylene glycol); Composite hydrogel; Antibacterial activity; Wound healing.

# 1.Introduction

The skin is the largest organ and first line of defense of the human body, and thus plays a crucial role in protecting the human body against external aggression, dehydration and electrolyte loss [1, 2]. However, skin damage, especially after bacterial infections such as Escherichia coli (*E. coli*) and Staphylococcus aureus (*S. aureus*), can easily lead to severe complications that hinder wound healing [3, 4]. Infections can get worse to sepsis and even osteomyelitis [5].

Various wound dressings have been developed to address these challenges, including hydrocolloid, nanofibers, beads and hydrogels [6-9]. Hydrogels, in particular, present great interest due to their outstanding permeability, biocompatibility, as well as moisture-retention and exudate absorption capacity [10-12]. Among them, chitosan-based hydrogels are most promising thanks to their intrinsic antibacterial properties [13]. In fact, the amino groups of chitosan can disrupt bacterial membranes via electrostatic interactions with the membranes' negatively charged components [14, 15]. Chitosan-based hydrogels can be obtained through physical or chemical crosslinking [16]. Physical hydrogels crosslinked via hydrogen bonding or electrostatic interactions generally have poor mechanical properties, which limits their application in wound healing [17, 18]. In contrast, the amino groups of chitosan allow for chemical crosslinking with other polymers bearing aldehyde groups via Schiff base reaction or carboxyl groups via esterification.

Metal-organic frameworks (MOFs) are porous materials assembled by inorganic clusters and organic ligands through strong coordination bonds [19], exhibiting unique advantages such as high specific surface area and tunable porosity [20]. Their applications span across various fields, including drug delivery [21], biosensing [22], antibacterial agents [23], and biocatalysis [24]. However, the instability of MOFs in protein-rich environments often leads to rapid ion release and increasing toxicity, which compromises long-term antibacterial effectiveness and limits their application in wound healing therapies [25, 26].

Glucose oxidase (GOx) is an oxido-reductase which catalyzes glucose oxidation to gluconic acid and hydrogen peroxide ($H_2O_2$). The latter is responsible for certain bactericidal effects observed in

biological systems, such as growth inhibition of one bacterial species by another and killing of invading microorganisms by activated phagocytic cells [27]. In the field of biology and medicine, GOx is mainly used in the preparation of nanomedicine for cancer diagnosis and treatment [28]. Despite its catalytic efficacy, it remains challenging to maintain the long-term catalytic activity of GOx during wound healing. Thus MOFs has been used as protective host for enzymes under harsh conditions, thereby stabilizing their activity [29].

This work aims to synthesize a novel chitosan-based GOx@Co-MOF composite hydrogel with pronounced antibacterial effect for wound healing applications. As depicted in Scheme 1, the composite hydrogel was prepared by crosslinking chitosan and aldehyde terminated di-functional poly(ethylene glycol) (DF-PEG) via Schiff base reaction, simultaneously incorporating GOx@Co-MOF. GOx can catalyze the decomposition of glucose to produce gluconic acid and $H_2O_2$, and Co-MOF can slowly release metal ions while protecting GOx. The resulting composite hydrogel exhibited outstanding antibacterial activity against both Gram-positive (*S. aureus*) and Gram-negative bacteria (*E. coli*). The potential of the composite hydrogel in promoting wound healing was evaluated through a series of experiments using a full-thickness wound mouse model.

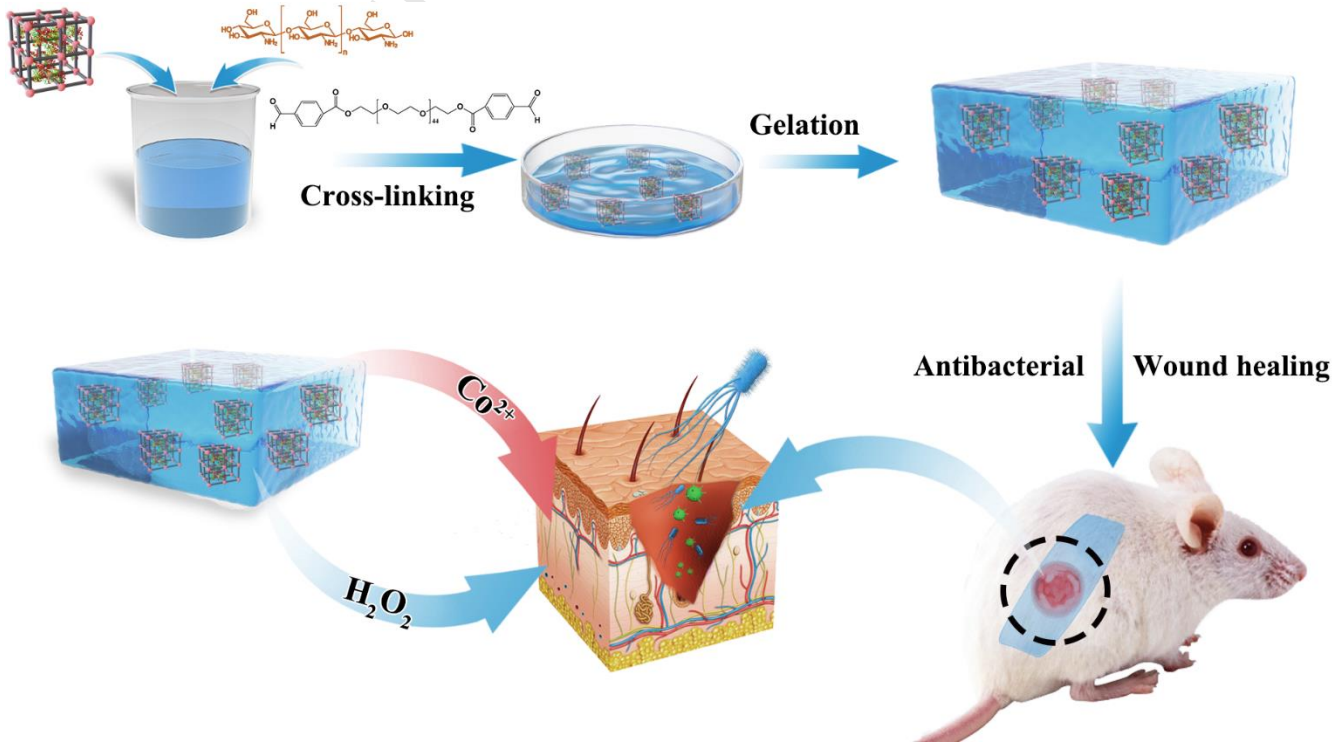

**Scheme 1.** Schematic presentation of CS/PEG/GOx@Co-MOF hydrogel preparation and its antibacterial and wound healing effects.

## 2.Materials and methods

### *2.1 Materials and reagents*

Cobalt nitrate hexahydrate ($Co(NO_3)_2 \cdot 6H_2O$, 99%), glucose oxidase (from Aspergillus Niger, >180 U/mg), chitosan (Mw 100 KDa, deacetylation degree ≥90%), tetrahydrofuran (99%), 4-dimethylaminopyridine (99%), N, N'-dicyclohexylcarbodiimide (99%), 4-formylbenzoic (98%), 2,2'-azino-bis (3-ethylbenzothiazoline-6-sulfonic acid) diammonium salt (ABTS) (98%) and horseradish peroxidase (HRP) (>200 U/mg) were obtained from Mucklin (Shanghai, China). TNF-α rabbit polyclonal antibodies (pAbs) and VEGF rabbit polyclonal antibodies (pAbs) were purchased from ABclonal (Wuhan, China). All other solvents were of analytical grade and used as received.

### *2.2 Synthesis of materials*

#### *2.2.1 Synthesis of GOx@Co-MOF*

GOx@Co-MOF was synthesized according to a literature method [30]. A sodium squaric solution (1.0 mL, 30.0 mg/mL, 0.14 M) was prepared in water, followed by addition of 2 mg of glucose oxidase. Meanwhile, a solution of cobalt nitrate hexahydrate (1.0 mL, 41.0 mg/mL, 0.14 M) was prepared in a water-ethanol mixture (15% ethanol). The two solutions were then mixed and allowed to react at room temperature for 30 min. The resultant product was isolated through centrifugation at 5000 rpm for 5 min, washing with water, and drying up to constant weight.

#### *2.2.2 Preparation of hydrogels*

Composite hydrogel was prepared according to a literature method with modifications [31]. Firstly, chitosan (0.15 g) was dissolved in acetic acid solution (5 mL, 1 wt%). 80 mg of the previously synthesized GOx@Co-MOF was then uniformly dispersed in the chitosan solution. Meanwhile, 1 g of DF-PEG with

Mn of 4000 was dissolved in 4 mL of deionized water. 0.5 mL of DF-PEG solution was then added to 0.5 mL of chitosan solution at room temperature. The mixture was subjected to vortexing, resulting in the formation of a GOx@Co-MOF composite hydrogel. For the sake of comparison, CS/PEG hydrogel, CS/PEG/GOx hydrogel, and CS/PEG/Co-MOF hydrogel were prepared using the same procedure without GOx@Co-MOF, Co-MOF or GOx, respectively. The obtained hydrogels were dialyzed for 24 h to remove non-crosslinked species for subsequent antibacterial, cell toxicity and animal experiments.

*2.3 Characterization*

Fourier transform infrared (FT-IR) spectra were obtained by Nicolet-IS50 FT-IR spectrometer using KBr pellets. The wavenumber range was 500 to 4000 $cm^{-1}$, and the number of scans was 32.

Scanning electron microscopy (SEM) was realized using JSM-7610F filed-emission SEM. Freeze-dried hydrogels and GOx@Co-MOF were gold-coated, and observed at 100× magnification using an electron beam at an accelerating voltage of 3 kV.

Energy dispersive spectroscopy (EDS) of hydrogels was performed using JSM-7610F filed-emission SEM under an electron beam acceleration voltage of 15.0 kV.

X-ray diffraction (XRD) spectra were registered using a Rigaku $d_{max}$ 2500 diffractometer with Cu Kα (λ = 1.5418 Å) in the range of 10− 40° 2θ at a speed of 1 s/step.

Thermogravimetric analysis (TGA) was performed using TG 209 F3 (Netzsch) under nitrogen atmosphere at a heating rate of 10 ℃ $min^{-1}$.

X-ray photoelectron spectroscopy (XPS) was performed on Escalab 250Xi (Thermo Fisher Scientific) using Al Kα as excitation source.

The compression properties of hydrogels were evaluated using TA Instruments Q800 series. Cylindrical hydrogel samples with a diameter of 2 cm and a height of 1 mm were prepared and tested at a strain rate of 1 mm/s.

The rheological properties of the hydrogels were determined by using a TA rheometer (DHR-2). Storage modulus (G') and loss modulus (G'') were measured at 25 °C from frequency sweeps in the 1-

100 Hz range and strain sweeps in the 0.1-100 % range.

*2.4 Swelling properties of hydrogel*

To evaluate the swelling properties, lyophilized hydrogels were immersed in pH 7.4 phosphate buffered saline (PBS) at 37°C. Periodically, the samples were recovered, and were weighed after removal of surface water. After reaching equilibrium, they were freeze-dried and weighed again.

The swelling and weight loss ratios of hydrogel samples are determined according to the following equations:

$$\text{Swelling ratio } (\%) = [(W_s - W_d)/W_d] \times 100$$

$$\text{Weight loss } (\%) = [(W_0 - W_d)/W_0] \times 100$$

where $W_0$ is the initial weight of freeze-dried hydrogel, $W_S$ is the wet weight of swollen hydrogel, and $W_d$ is the dried weight of remaining hydrogel.

*2.5 Detection of $H_2O_2$ and enzyme activity of GOx*

*2.5.1 Detection of $H_2O_2$*

The release of $H_2O_2$ from GOx@Co-MOF and composite hydrogels was measured using a hydrogen peroxide content detection kit (Solarbio, China). Co-MOF, GOx@Co-MOF, CS/PEG hydrogel and CS/PEG/GOx@Co-MOF composite hydrogel were added to a glucose solution (0.5 wt%), respectively. After preset time periods, the supernatant was collected, and the absorbance was measured at a wavelength of 415 nm.

*2.5.2 Enzyme activity of free GOx and GOx@Co-MOF*

3 mL of catalytic system were prepared in pH 7.4 PBS (0.1M), including ABTS (10 mM, 100 μL), glucose (1 wt%, 300 μL), HRP and GOx (1 mg/mL, 31 μL) or GOx@Co-MOF (17 mg/mL, 31 μL). The enzyme concentration in both GOx and GOx@Co-MOF groups was 10 μg/mL. The activity of GOx was monitored at 734 nm using UV–vis spectrophotometry. The concentration of $ABTS^{\bullet+}$ was calculated

according to Beer-Lmbert Law, using the molar absorption coefficient of $1.5\times10^4$ $M^{-1}cm^{-1}$ [32]. The catalytic rate was determined from the average rate in the first 2 min.

*2.6 Bacterial culture and antimicrobial test*

The antibacterial effect of CS/PEG/GOx@Co-MOF composite hydrogels was evaluated by tests against Gram-positive bacteria (*S. aureus*) and Gram-negative bacteria (*E. coli*). Fresh cultures were prepared by isolating single colonies from Luria-Bertani (LB) plates, and incubated at 37 ℃ for 12 h in 10 mL of sterile LB medium under shaking at 175 rpm. After reaching the logarithmic growth phase, the bacterial cultures were diluted to a concentration of $10^6$ colony-forming units per milliliter (CFU/mL) using PBS.

50 μL of the above diluted bacterial solution were first coated on LB solid medium containing glucose (0.5 wt%). Then, 40 μL of CS/PEG, CS/PEG/GOx, CS/PEG/Co-MOF and CS/PEG/GOx@Co-MOF samples were added to the center of the solid medium. The inhibition zone was measured after 12, 24, and 48 h incubation at 37 ℃.

For the growth-inhibition assay, *E. coli* and *S. aureus* in the logarithmic growth phase were diluted to $1.0\times10^5$ CFU/mL in LB liquid medium. 200 μL of hydrogel samples were placed in a 24-well plate. 100 μL of bacterial suspension and 900 μL of LB medium were added to the surface of each sample, and then incubated at 37 ℃. A small amount of bacterial liquid was extracted for live-dead bacterial staining experiments and agar plate experiments after 24 h.

*2.7 Cytotoxicity test*

The cytotoxicity of GOx@Co-MOF and hydrogels was evaluated by MTT assay on L929 cell line. GOx@Co-MOF were uniformly dispersed in a complete culture medium. CS/PEG and CS/PEG/GOx@Co-MOF hydrogels were sterilized under UV radiation for 1 h, and then soaked in complete culture medium. After 24 h incubation at 37 ℃, the cell suspension was seeded into a 96-well plate at a density of $1\times10^5$ cells per well, and incubated at 37°C in a 5% $CO_2$ atmosphere. After preset

incubation periods, the culture medium was replaced with the medium containing the test samples, and cell viability was assessed using MTT assay.

In addition, live-dead cell staining was conducted to further evaluate the cytotoxicity of hydrogels. Live-dead cell staining was performed using acridine orange/propidium iodide (AO/PI) double staining kit (Beijing Biolab Technology Co., Ltd.). L929 cells were cultured in 24-well plates at a density of $1\times10^5$ cells/mL for 24 h. The cell culture medium was then replaced with 1 mL of GOx@Co-MOF suspension (50 μg/mL) or hydrogels extract (500 μg/mL), respectively. After 24 h incubation, the culture medium was discarded and washed with sterile PBS. Complete medium containing AO and PI was then added, incubated in the dark for 20 min, washed with PBS and imaged with an inverted fluorescence microscope.

*2.8 In vivo tests*

*2.8.1 Mouse model establishment*

All animal experiments were performed in accordance with the guidelines of the National Research Council's Guide for the Care and Use of Laboratory Animals. In vivo full-thickness skin defect model was used to evaluate the effect of hydrogels to promote wound healing [33]. Institute of Cancer Research mice (30-35 g) aged 6-7 weeks were divided into five distinct groups, including control (PBS), GOx@Co-MOF, CS/PEG hydrogel, CS/PEG/Co-MOF hydrogel, and CS/PEG/GOx@Co-MOF hydrogel groups. The mice's back was carefully shaved, followed by the creation of a full-thickness wound using surgical scissors. Subsequently, the wounds were infected with a S. aureus suspension (20 μL, $1.0\times10^7$ CFU/mL) to establish a bacterial infection model. After 24 h, each wound was treated with 30 μL of the various dressings. The dressings were changed and wound healing was checked on day 1, 5, 9, 15, 19 and 22. The wound area was recorded with a camera and calculated with image processing software (Image J) according to the following formula:

$$\text{Wound area } (\%) = [(A_0 - A_t) / A_0] \times 100$$

where $A_0$ is the original wound area, and $A_t$ is the wound area at the time of examination.

*2.8.2 Wound bacteria content*

Mouse wound tissues were excised on day 22, homogenized in LB medium, and co-incubated at 37 ℃ for 5 h [34]. Then the bacteria-containing solution was diluted $1.0\times10^3$ times, and cultured on solid LB medium at 37 ℃ for 24 h. Finally, the number of colonies was counted for quantitative analysis.

*2.8.3 Histology and immunohistochemistry*

At the end of 22 days, all mice were executed from each group for histological and immunohistochemistry analyses. Wound regeneration and healing processes were evaluated using Hematoxylin-Eosin (H&E) and Masson's trichrome staining techniques. For this purpose, the collected mouse wound tissue samples were fixed with 4% paraformaldehyde, embedded in paraffin, and then sectioned into 5 μm thick slices. The latter were dehydrated with xylene and ethanol, and stained with H&E and Masson's trichrome dye [1, 33]. The stained sections were then meticulously observed, analyzed, and imaged using an IX53 Olympus microscope.

Immunohistochemical staining was performed to probe the expression of specific biomarkers. The process began with high-pressure antigen retrieval using a 10 mM citrate buffer (pH 6.0). Staining was then performed with TNF-α rabbit antibody and VEGF rabbit antibody diluted 1:100 (40×). Afterwards, the tissue sections were dehydrated with ethanol, embedded in paraffin, and were examined under a microscope.

*2.9 Statistical analysis*

All experimental procedures were repeated three times (n = 3) to ensure reliability and reproducibility of the data. The results are presented as the mean ± standard deviation. Statistical analyses were conducted using GraphPad Prism software (version 8.0). Analysis of Variance (ANOVA) tests were employed to determine the level of significance and p values.

**3. Results and discussion**

*3.1 Characterization of GOx@Co-MOF*

GOx@Co-MOF was characterized using various analytical techniques. As shown in Fig. 1a, the XRD pattern of GOx@Co-MOF well agrees with that of pristine Co-MOF, affirming the structural integrity of the samples. The FT-IR spectrum of GOx@Co-MOF reveals distinct characteristic signals (Fig. 1b). The broad absorption peak ranging from 3750 to 3000 $cm^{-1}$ is attributed to the stretching vibrations of the O-H groups. The peak near 1500 $cm^{-1}$ is mainly associated with C=C stretching vibrations, while the peak at 1102 $cm^{-1}$ belongs to the C-O stretching vibrations [35]. A significant observation is the presence of the peak at 1640 $cm^{-1}$ in the GOx@Co-MOF spectrum, which is attributed to the -CO-NH- bond stretching vibrations, suggesting the successful incorporation of the GOx enzyme within the Co-MOF structure. SEM shows that GOx@Co-MOF has a cube structure with a size of 10-20 μm (Fig. 1d), which is slightly larger than that of pristine Co-MOF (Fig. 1c).

The thermal stability of GOx@Co-MOF was assessed by using TGA (Fig. 1e). Approximately 5% of mass loss was observed below 150 ℃, which is attributed to the evaporation of adsorbed water. A significant weight loss of 20.3% between 200°C and 320°C was attributed to the loss of structural water and GOx. Compared with Co-MOF, GOx@Co-MOF has slightly larger weight loss at this weight loss step, in agreement with the incorporation of GOx. The mass loss above 320 ℃ results from the decomposition of the MOF structure.

XPS analysis shows that the composite contains C, N, O, S and Co elements (Fig. 1f). As shown in Fig. 1g, the XPS spectrum of C1s has three main peaks at 284.6, 286.4 and 288.4 eV, which are assigned to C-C, C-(N, O) and C=C, respectively [36, 37]. The nitrogen spectrum (Fig. 1h) shows two peaks at 399.7 and 401.7 eV, corresponding to N–C=O and N–H bonds, respectively [38]. The cobalt spectrum (Fig. 1i) presents two peaks at 781.9 and 797.8 eV, corresponding to the binding energies of Co 2p3/2 and Co 2p1/2, along with satellite peaks associated with the shakeup excitation of $Co^{2+}$ ions [39, 40]. All these data demonstrate the successfully synthesis of GOx@Co-MOF crystals.

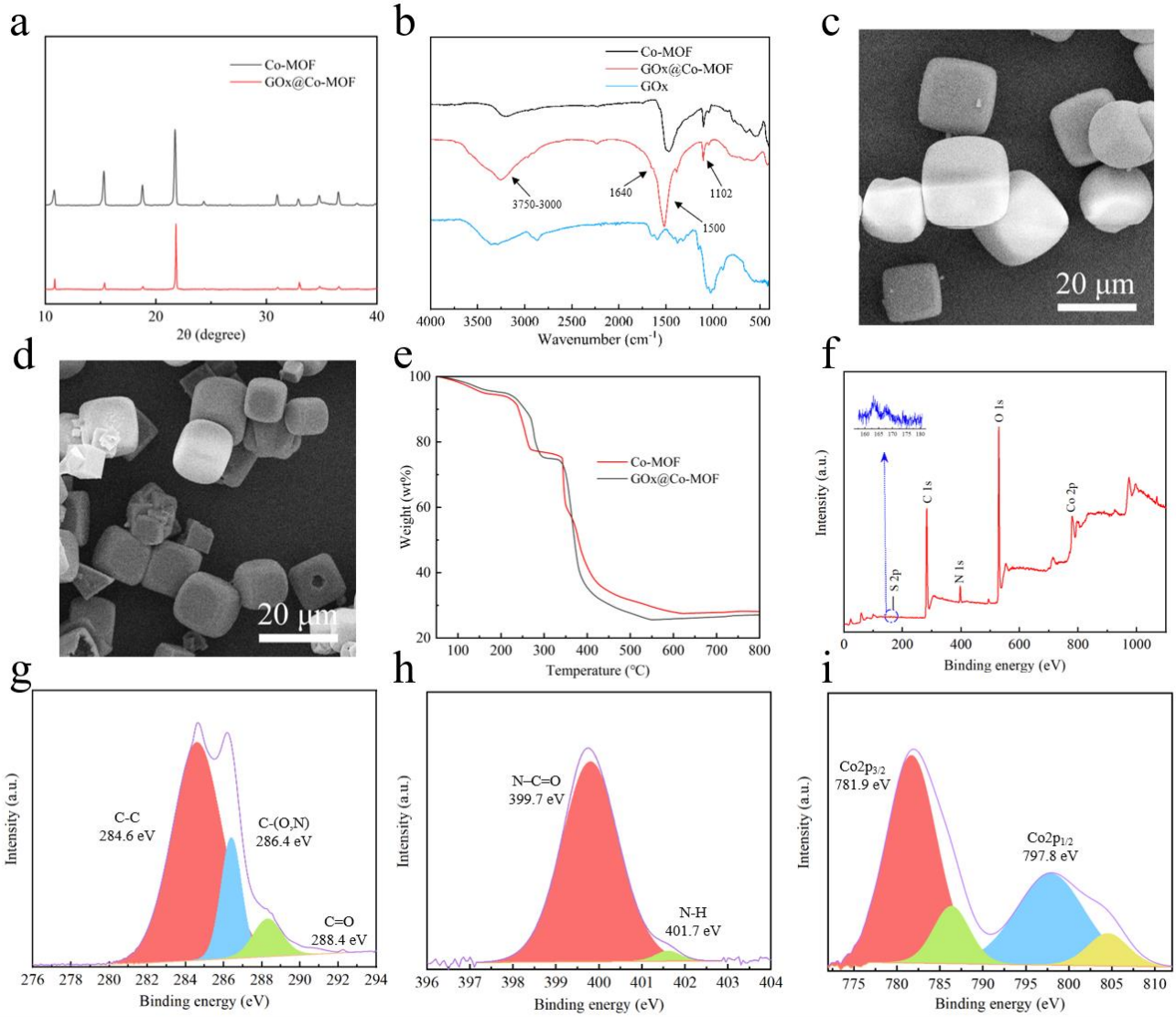


**Fig.1** Characterization of GOx@Co-MOF: (a) XRD pattern of GOx@Co-MOF; (b) Infrared spectra of Co-MOF, GOx@Co-MOF and GOx; (c) SEM image of Co-MOF; (d) SEM image of GOx@Co-MOF; (e) TGA thermograms of Co-MOF and GOx@Co-MOF; (f-i) XPS survey spectrum and high-resolution C 1s, N 1s, and Co 2p spectra of GOx@Co-MOF.

*3.2 Characterization of hydrogels*

PEG was first functionalized with 4-formylbenzoic acid in the presence of DCC/DMAP as coupling agents (synthesis method in Supplementary data). The resulted di-functional PEG (DF-PEG) with aldehyde groups at the chain ends was characterized by FT-IR and NMR (Fig. S1). News signals are detected on the FT-IR and NMR spectra of DF-PEG as compared to those of PEG, thus confirming the

successful functionalization of PEG.

GOx@Co-MOF loaded composite hydrogel was synthesized through crosslinking of CS and DF-PEG via Schiff base reaction. The structural characterization of CS/PEG/GOx@Co-MOF hydrogel was performed using various analytical techniques, in comparison with CS/PEG hydrogel. The XRD pattern (Fig. 2a) of CS/PEG hydrogel reveals the diffraction peaks of PEG at θ = 10.9°, 15.5°, 19.1° and 23.1°. A new diffraction peak was detected at θ = 21.8° on the spectrum of CS/PEG/GOx@Co-MOF hydrogel, which proves that that the GOx@Co-MOF structure remains intact within the hydrogel matrix. As shown in Fig. 2b, the FT-IR spectra of CS/PEG and CS/PEG/GOX@Co-MOF hydrogels contain various characteristic signals of CS and DF-PEG, among which the peak at 3490 $cm^{-1}$ belongs to the stretching vibration of O-H and N-H, and the peak at 2882 $cm^{-1}$ to the stretching vibration of C-H. The peak at 1104 $cm^{-1}$ is assigned to the stretching vibration of C-O [41]. The peaks at 1717 and 1643 $cm^{-1}$ belong to the remaining aldehyde groups and newly formed imine bonds, which confirms the formation of hydrogels by cross-linking of DF-PEG and CS via Schiff base reaction.

SEM provides insights into the morphological aspects of the hydrogels (Fig. 2c). The freeze-dried CS/PEG/GOx@Co-MOF hydrogel exhibits a dense honeycomb structure, which appears more compact compared to the CS/PEG hydrogel (Fig. S2). Importantly, structurally intact GOx@Co-MOF particles are evenly distributed in the wall of the hydrogel network (Fig. S3a-b).

TGA was used to evaluate the thermal stability of freeze-dried CS/PEG and CS/PEG/GOx@Co-MOF hydrogel. The small weight loss below 100 ℃ is attributed to the removal of free water, while the weight loss from 100 to 260 ℃ (4.2% for CS/PEG and 6.3% for CS/PEG/GOx@Co-MOF) is attributed to the removal of bound water and short chain decomposition of CS. The mass loss from 260 ℃ to 450 ℃ (77.8% for CS/PEG and 73.8% for CS/PEG/GOx@Co-MOF) is mainly due to the decomposition of DF-PEG and CS. The weight loss over 320 ℃ also includes the decomposition of GOX@Co-MOF.

According to the XPS survey spectrum, the CS/PEG/GOx@Co-MOF hydrogel is composed of C, N, O, S, and Co elements (Fig. S4). The high-resolution XPS spectra are shown in Fig. 2e and 2f. The three peaks of C 1s at 384.6, 386.1 and 387.7 eV are assigned to C-C, C-(N, O) and C=C, respectively,

whereas the two peaks of O 1s at 530.7 and 531.3 eV are ascribed to C=O and O-H.

EDS analysis was utilized to verify the successful incorporation of GOx@Co-MOF within the hydrogel. As shown in Fig. 2g, C, Co and S elements are evenly distributed, indicating that GOx@Co-MOF is successfully doped and evenly distributed in the hydrogel.

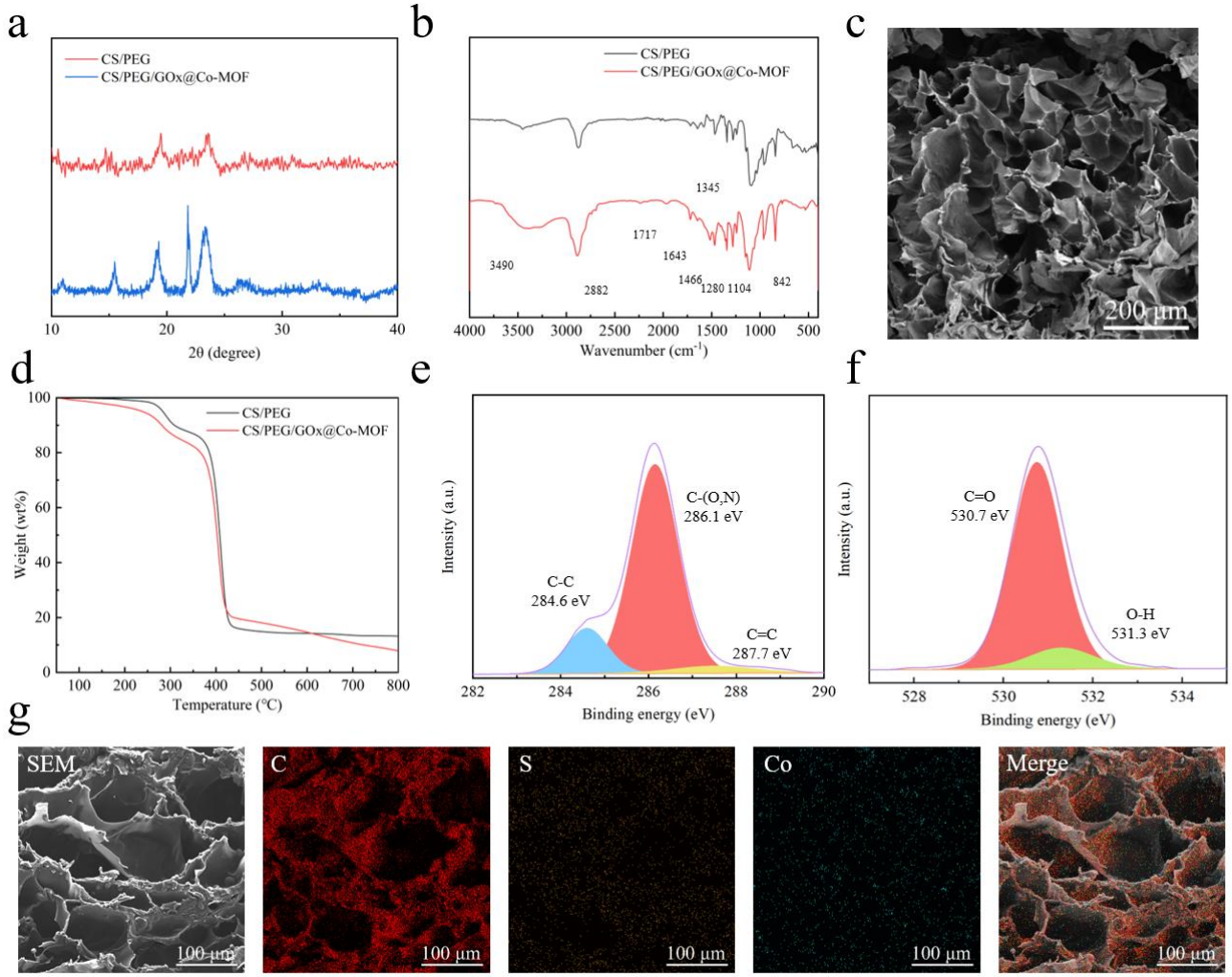


**Fig.2** Characterization of CS/PEG and CS/PEG/GOx@Co-MOF hydrogels: (a) XRD patterns and (b) infrared spectra of CS/PEG and CS/PEG/GOx@Co-MOF hydrogels; (c) SEM image of CS/PEG/GOx@Co-MOF hydrogel; (d) TGA thermograms of CS/PEG and CS/PEG/GOx@Co-MOF hydrogels; (e-f) High-resolution C 1s and O 1s spectra of CS/PEG/GOx@Co-MOF hydrogel; (g) SEM-EDS images of CS/PEG/GOx@Co-MOF hydrogel (from left to right, SEM image, elemental mapping of C, S and Co, and Marge image).

*3.3 Swelling behaviors of hydrogels*

Excessive production of wound exudate can lead to maceration of uninjured skin adjacent to the wound [42]. Proper swelling properties can provide a moist environment conducive to wound healing and wound exudate absorption [17]. As illustrated in Fig. 3a, the swelling ratio of CS/PEG/GOx@Co-MOF hydrogel (*c.a* 2040%) is lower than that of CS/PEG hydrogel (*c.a* 3690%). This may be attributed to the more compact structure of the former due to the presence of GOx@Co-MOF. Fig. 3b shows the weight loss of hydrogels after swelling. A weight loss of 21.1% is observed for CS/PEG/GOx@Co-MOF hydrogel, which is lower than that of CS/PEG hydrogel (32.5%). The weight loss mainly results from the washing away of non-crosslinked species. The swelling behavior reveals that CS/PEG/GOx@Co-MOF hydrogel is able to absorb exudates and maceration of wound.

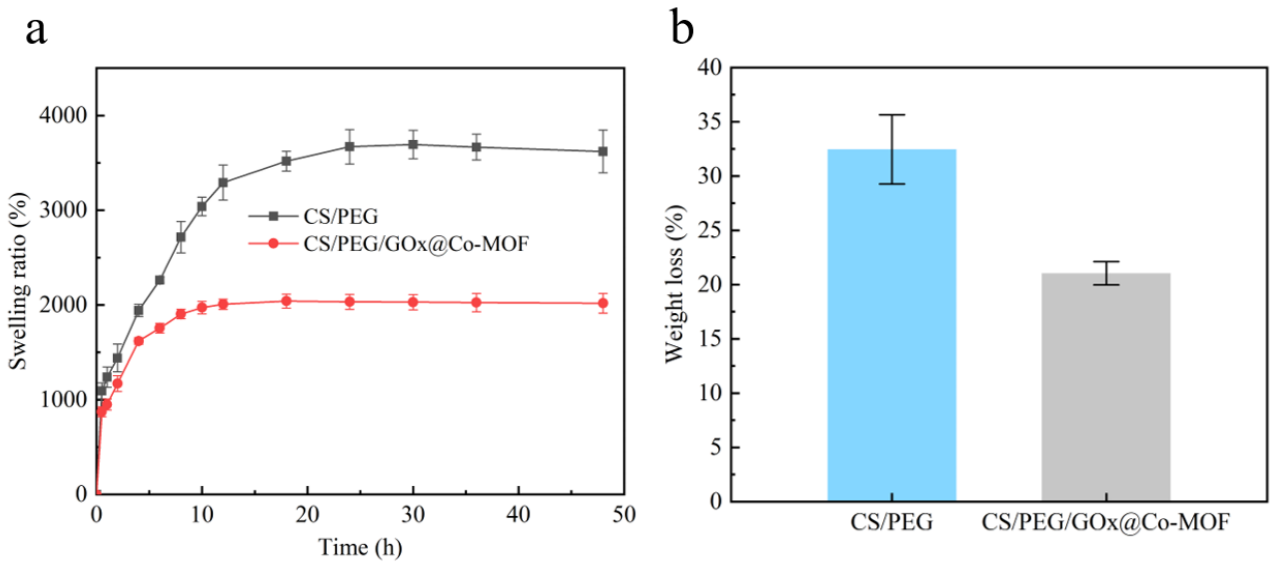


**Fig. 3** (a) Swelling ratio changes and (b) weight loss percentages of CS/PEG and CS/PEG/GOx@Co-MOF hydrogels during 48 h swelling.

*3.4 Rheological properties of hydrogel*

The rheological properties of hydrogels were determined to evaluate their mechanical performance which is of crucial importance for skin wound repair. Fig. 4a shows the changes of the storage modulus (G') and loss modulus (G") as a function of frequency. The G' of CS/PEG/GOx@Co-MOF and CS/PEG is higher than the G" in the whole frequency range, indicating that both are in the state of hydrogel. On the other hand, the G' and G" of CS/PEG/GOx@Co-MOF are higher than those of CS/PEG hydrogel, in

agreement with the more compact structure of the former. Fig. 4b shows the change of G' and G" of the two hydrogels as a function of applied strain. G' and G" remain almost unchanged up to a strain of 100%, indicating that both hydrogels have good structural stability due to covalent crosslinking via Schiff base reaction.

As a skin wound healing material, hydrogel needs to have a certain mechanical strength to resist external forces. As shown in Fig. 4c, CS/PEG/GOx@Co-MOF and CS/PEG hydrogels have similar stress distributions, and the maximum stress of CS/PEG/GOx@Co-MOF hydrogel (10.7 kPa) is significantly higher than that of CS/PEG hydrogel (6.6 kPa).

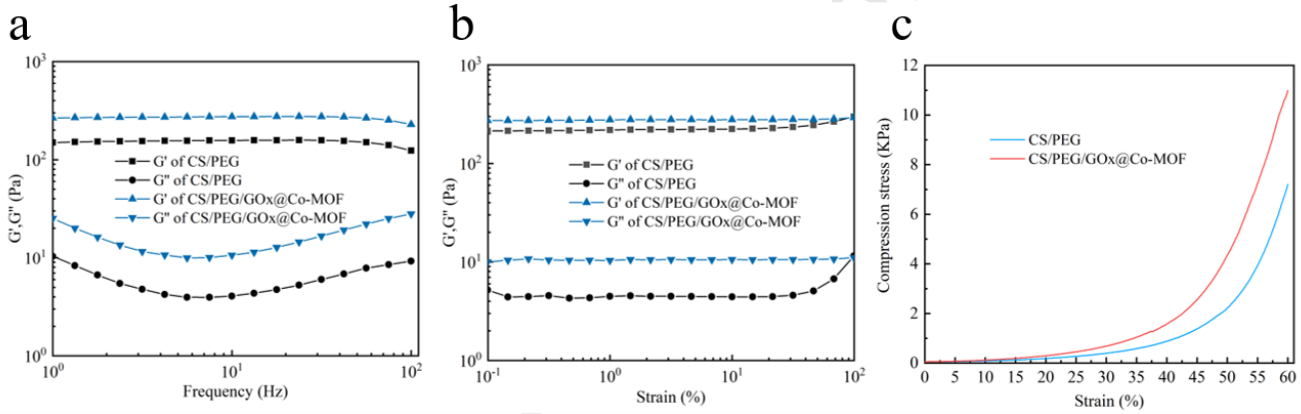


**Fig. 4** Storage modulus (G') and loss modulus (G") changes as a function of frequency (a) and strain (b), compressive stress versus strain curves (c) of CS/PEG and CS/PEG/GOx@Co-MOF hydrogels.

The CS/PEG and CS/PEG/GOx@Co-MOF hydrogels exhibit remarkable self-healing properties (Fig. S5a-b). The interface of two semi-circular hydrogels became integrated after one hour at room temperature. This healed hydrogel, upon two-hour immersion in PBS (50 mM, pH 7.0), maintains its shape, suggesting dynamic functional group interactions rather than mere adhesion at the fracture interface. Rheological measurements post self-healing (Fig. S5c) reveals that both G' and G" remain nearly the same, indicating that the hydrogel retains its mechanical strength post-healing.

*3.6 Detection of hydrogen peroxide ($H_2O_2$)*

GOx can catalyze glucose oxidation to produce $H_2O_2$, and ABTS can react quickly with hydroxyl

radicals to produce colored $ABTS^{\bullet+}$. The enzymatic activity of GOx and GOx@Co-MOF was determined using ABTS colorimetric assay. As shown in Fig. S6a, the $ABTS^{\bullet+}$ concentration rapidly increased in the first 10 min, and then levelled off. The catalysis rate of free GOx and immobilized GOx was 12.1 and 3.1 mM/min, respectively (Fig. S6b).

Then, the catalytic activity of GOx@Co-MOF and CS/PEG/GOx@Co-MOF hydrogel was determined by using glucose solution (0.5 wt%). The concentration of produced $H_2O_2$ was measured using a hydrogen peroxide content detection kit (Solarbio, China). As shown in Fig. 5a, a constant increase in $H_2O_2$ concentration is observed for both GOx@Co-MOF and CS/PEG/GOx@Co-MOF hydrogel groups, whereas the concentration remains very low for Co-MOF and CS/PEG taken as controls. GOx@Co-MOF group shows higher catalysis rate (0.08 mM/min) than GOx@Co-MOF immobilized in hydrogel (0.04 mM/min), as shown in Fig. 5b.

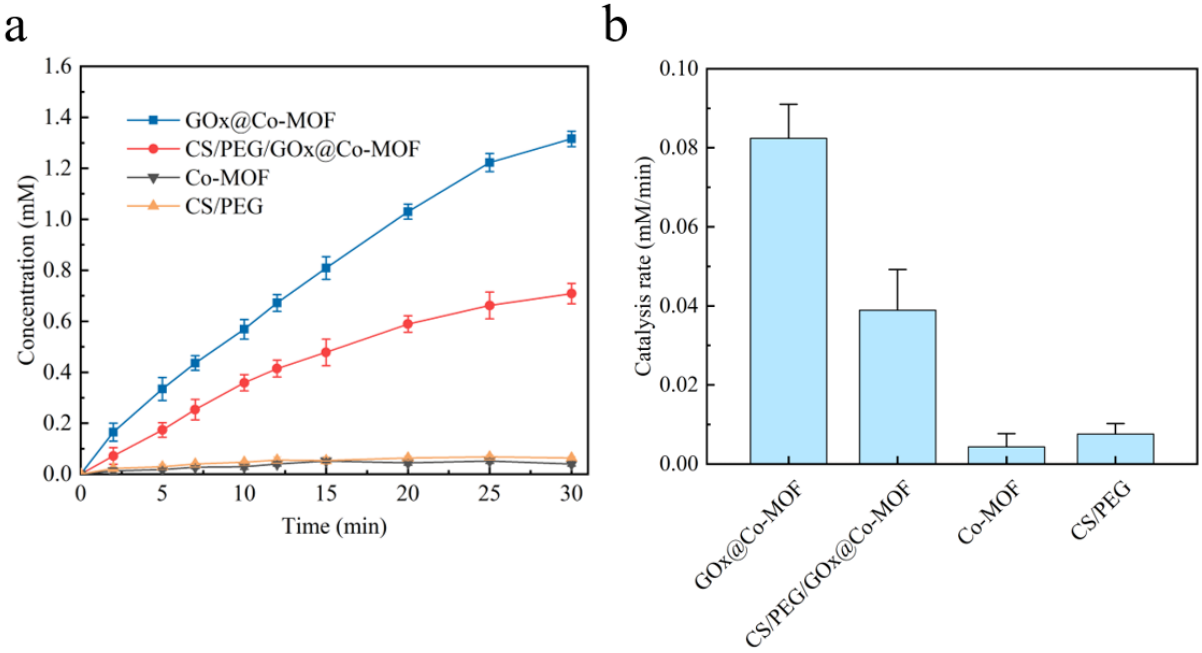


**Fig. 5** $H_2O_2$ concentration changes as a function of time (a), and catalysis rates (b) of GOx@Co-MOF, CS/PEG/GOx@Co-MOF hydrogel, Co-MOF, and CS/PEG hydrogel.

*3.7 Antimicrobial property of hydrogel*

Wounds exposed to the external environment are susceptible to bacterial infections such as *E. coli* and *S. aureus*, resulting in slower wound healing. As shown in Fig. 6a, CS/PEG/GOx@Co-MOF

hydrogel has the best antibacterial effect and the longest antibacterial time. In contrast, the inhibition zones of CS/PEG hydrogel, CS/PEG/GOx hydrogel and CS/PEG/Co-MOF hydrogel were smaller and significantly reduced at 48 h. The CS/PEG/GOx hydrogel has no obvious antibacterial effect, which may be due to the inactivation of GOx. Owing to the protection effect of the rigid frameworks of MOFs [43], GOx can preserve good antibacterial activity in CS/PEG/GOx@Co-MOF hydrogel. As shown in Fig. 6b-c, the sustained antibacterial activity assay also proved that CS/PEG/GOx@Co-MOF hydrogel has long-acting antibacterial activity. According to the plate count method, the CS/PEG/GOx@Co-MOF hydrogel group had the least number of colonies after 48 h of liquid culture (Fig. 6d-e). Bacterial staining assay shows that the CS/PEG/GOx@Co-MOF hydrogel has higher long-lasting antibacterial effect than other controls (Fig. 6f), which might be attributed to the synergy of $Co^{2+}$ released from Co-MOF and $H_2O_2$ produce by GOx [44, 45].

The release of $Co^{2+}$ from Co-MOF, GOx@Co-MOF suspensions and CS/PEG/GOx@Co-MOF hydrogel was evaluated in PBS at 25 ℃. ICP-OES results showed that $Co^{2+}$ was rapidly released from Co-MOF and GOx@Co-MOF, reaching a concentration of 12.8 and 12.1 μg/mL at 30 min, respectively (Fig. S7a). In contrast, a nearly constant increase of $Co^{2+}$ concentration is observed for CS/PEG/GOx@Co-MOF hydrogel with the same MOF content, reaching 8.6 μg/mL at 48 h (Fig. S7b). The finding suggests that hydrogel has a sustaining effect on $Co^{2+}$ release, allowing to prolong the action time of the composite hydrogel.

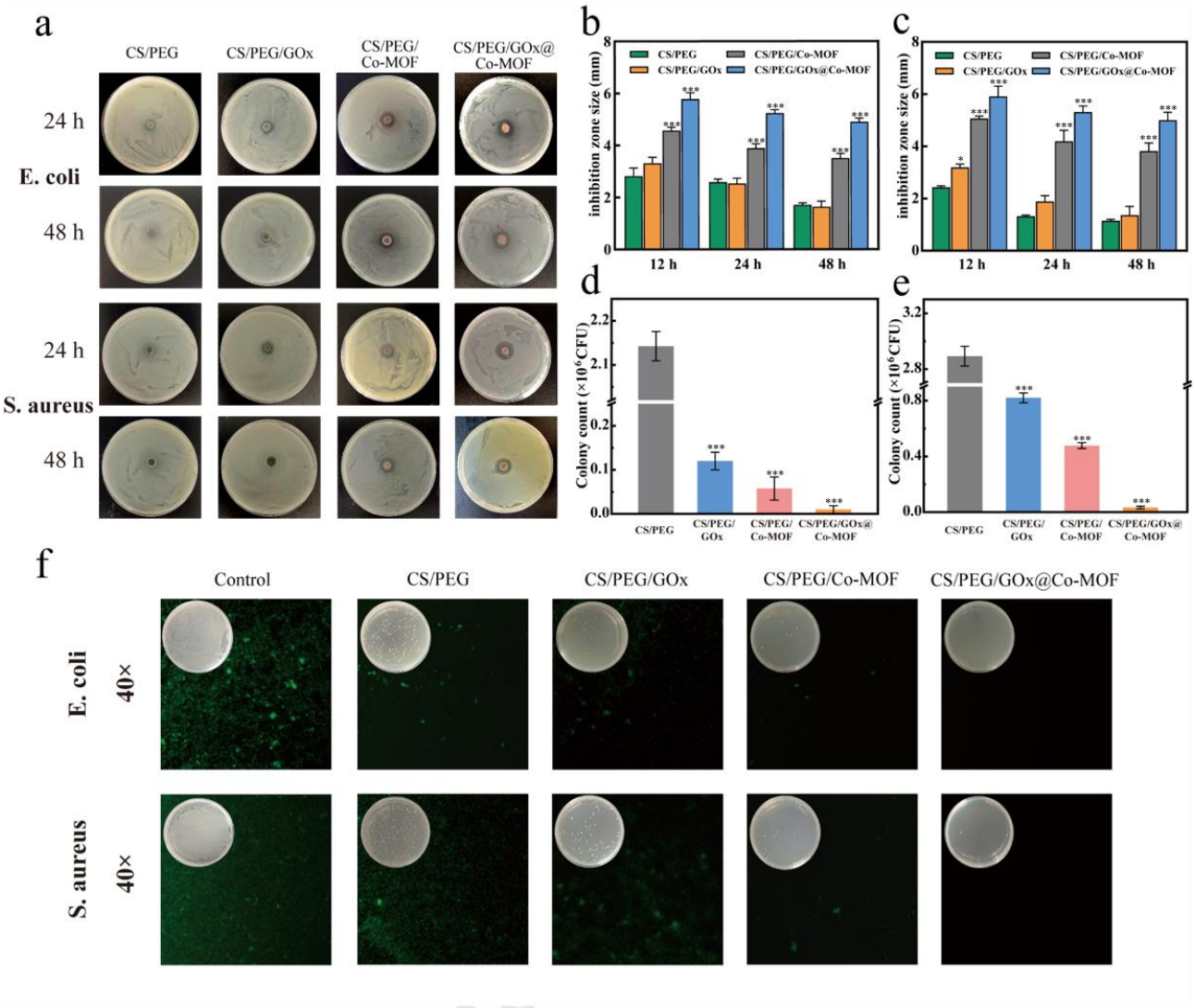


**Fig. 6** Inhibition zone pictures of CS/PEG, CS/PEG/GOx, CS/PEG/Co-MOF and CS/PEG/GOx@Co-MOF hydrogels against *E. coli* and *S. aureus* (a); Inhibition zone size of hydrogels against *E. coli* (b) and *S. aureus* (c); Number of colonies after 48 h liquid culture with *E. coli* (d) and *S. aureus* (e); Live/dead staining of *S. aureus* and *E. coli* after co-culture with the hydrogels for 24 h (f). The inset digital photos show the bacterial colonies of *S. aureus* and *E. coli* on agar plates for 24 h. (n = 3, *p < 0.05, **p < 0.01, ***p < 0.001)

*3.8 Cytotoxicity test*

Favorable cell compatibility is a prerequisite for designing novel wound dressing materials [46]. As shown in Fig. 7a-b, GOx@Co-MOF and CS/PEG/GOx@Co-MOF hydrogel present good biocompatibility. In the range of 5-50 μg/mL, the cell survival rate was above 90% after 24 h co-

incubation with GOx@Co-MOF, and slightly decreased after 48 h (>80%). In the case of CS/PEG/GOx@Co-MOF hydrogel, the cell survival rate is higher than 95% in the range of 10-300 μg/mL at 48 h, and above 85% after 72 h.

GOx@Co-MOF, CS/PEG hydrogel and CS/PEG/GOx@Co-MOF hydrogel samples were incubated with L929 cells for 24 h and stained with AO/PI kit. As shown in Fig. 7c, no apoptosis is observed for cells incubated with the CS/PEG and CS/PEG/GOx@Co-MOF hydrogel groups as in the case of the control, and the cells exhibit spherical, spindle, or elongated shape. Meanwhile, weak red fluorescence appeared in the GOx@Co-MOF group, this may be attributed to the rapid release of $H_2O_2$ and $Co^{2+}$ without hydrogel. According to the United States Pharmacopoeia Standards, it is concluded that the CS/PEG/GOx@Co-MOF hydrogel has good biocompatibility and presents great potential as wound dressing.

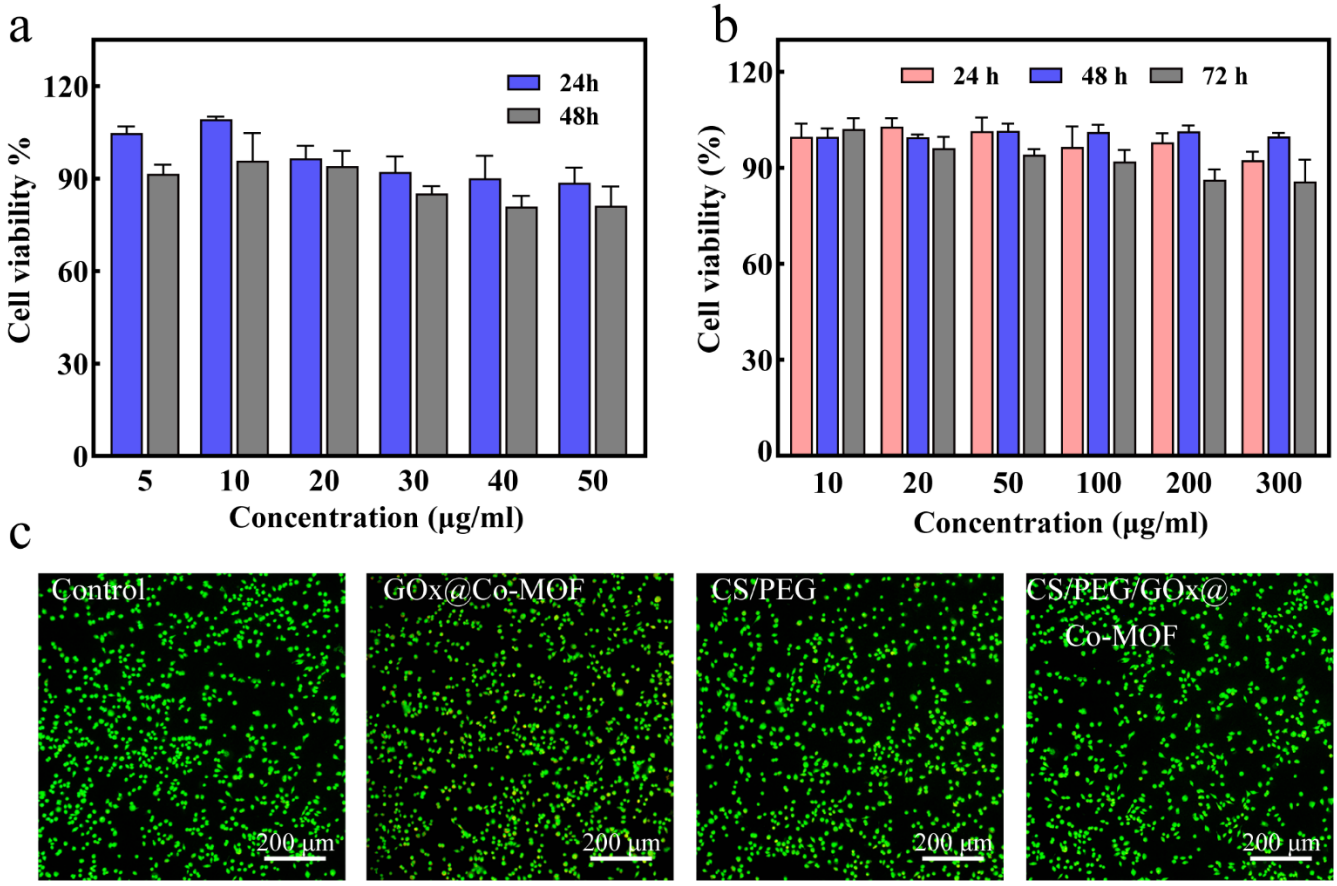


**Fig. 7** (a) Cell viability of L929 cells after 48 h incubation with GOx@Co-MOF; (b) Cell viability of L929 cells after 72 h incubation with CS/PEG/GOx@Co-MOF hydrogel; (c) Fluorescent images of L929 cells after treatment with GOx@Co-MOF (50 μg/mL), CS/PEG hydrogel (300 μg/mL) and

CS/PEG/GOx@Co-MOF hydrogel (300 μg/mL) in comparison with control.

*3.9 Mouse model studies*

A mouse model featuring full-thickness infected wounds, each 7 mm in diameter, was established to evaluate the effect of CS/PEG/GOx@Co-MOF hydrogel on wound healing, in comparison with GOx@Co-MOF, CS/PEG hydrogel, CS/PEG/Co-MOF hydrogel, and PBS taken as control. Rapid wound closure was observed in the CS/PEG/GOx@Co-MOF hydrogel group, with most wounds substantially healed by day 15, as depicted in Fig. 8a-c. While wounds in the PBS group exhibited exacerbated conditions by day 5 probably due to bacterial infection, and remained unhealed until day 22. Compared to wound dressings and marketing material (Tegaderm™ film) reported in literature, CS/PEG/GOx@Co-MOF hydrogel presents faster or comparable wound healing rate (Table S1). The amount of released $H_2O_2$ is dependent on the glucose content at the wound site, allowing to enhance the antibacterial activity and to prevent irritation.

Assessment of wound bacterial contents revealed that the CS/PEG/GOx@Co-MOF hydrogel group had the lowest bacterial count ($0.024\times10^5$ CFU/mL), significantly lower than the PBS ($6.07\times10^5$ CFU/mL), GOx@Co-MOF ($1.0\times10^5$ CFU/mL), CS/PEG hydrogel ($3.33\times10^5$ CFU/mL) and CS/PEG/Co-MOF hydrogel ($0.12\times10^5$ CFU/mL) groups, as shown in Fig. 8d-e. These findings demonstrate the potent wound antibacterial properties of CS/PEG/GOx@Co-MOF hydrogel, presumably due to the sustained release of $H_2O_2$ and $Co^{2+}$.

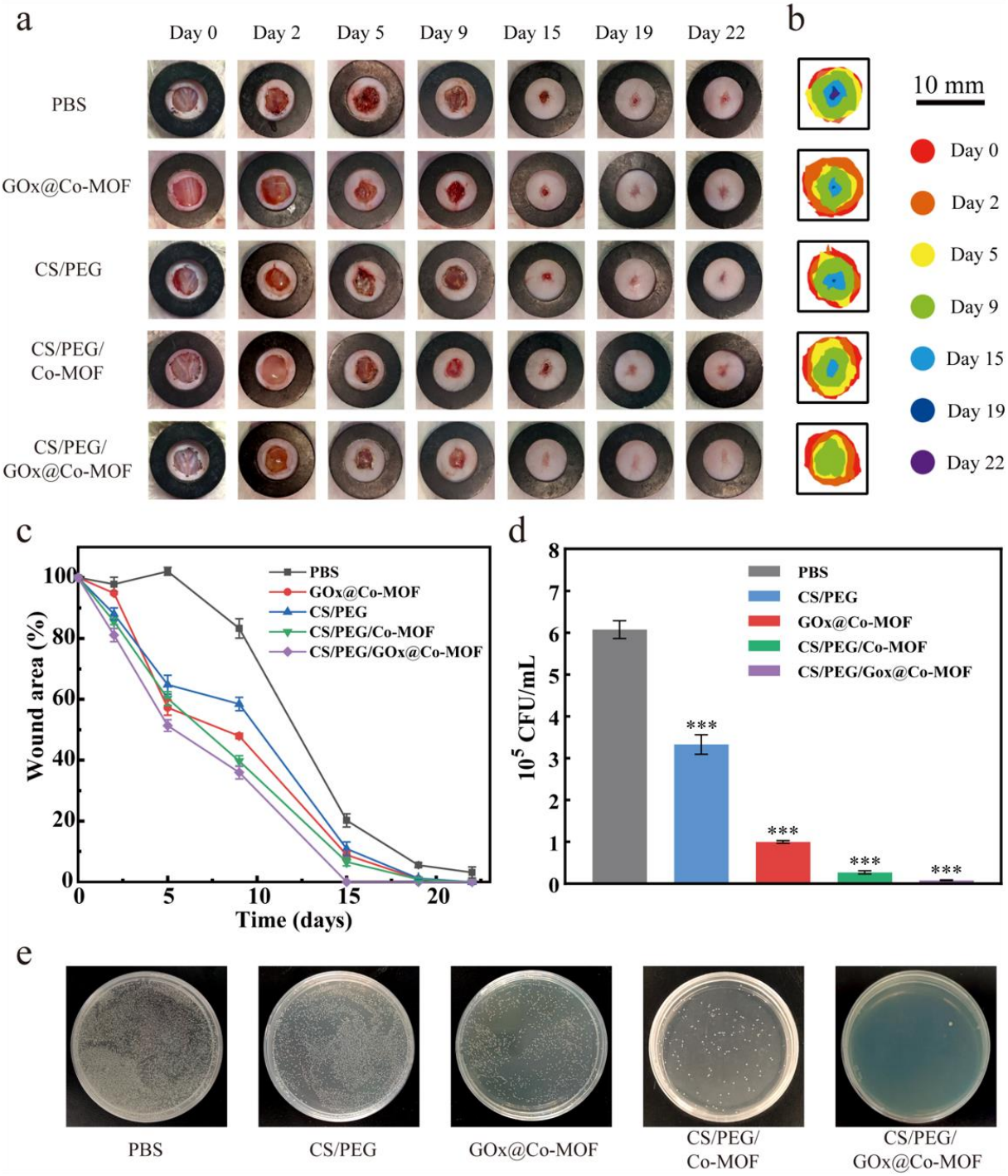


**Fig. 8** Photographs of S. aureus-infected wounds on mice after treatment at different times; (b-c) Relative wound area of mice after different treatments; Colony number (d) and photos (e) of surviving bacteria in the wound tissue after 24 h culture on solid LB medium at 37 ℃. (n = 3, *p < 0.05, **p < 0.01, ***p < 0.001)

Histological and immunohistochemical examinations were carried out to evaluate the regeneration and healing of wounds in various groups. In order to further evaluate the inflammatory response and

angiogenesis of the tissues, the skin tissues after 22 days of treatment were analyzed histologically by H&E and Masson's trichrome staining. Fig. 9a shows the micrographs of H&E stained wounds in different treatment groups. Compared to the other groups, the CS/PEG/GOx@Co-MOF hydrogel group had more mature granulation tissue, tighter collagen fibers, and evenly distributed blood vessels around the wound. Masson's trichrome staining was used to further analyze the collagen deposition in the healing wounds. As shown in Fig. 9b, the CS/PEG/GOx@Co-MOF hydrogel group can improve the deposition of collagen in the granulation tissue. The collagen deposition appears denser and more organized than in other groups. In summary, these results show that the CS/PEG/GOx@Co-MOF hydrogel could better promote wound closure.

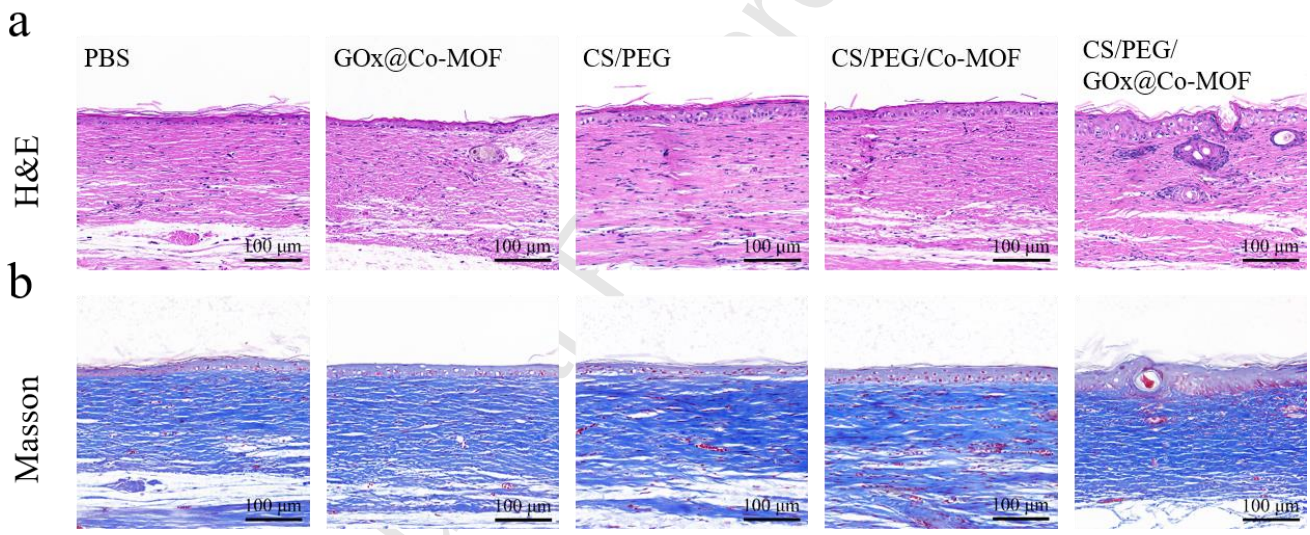


**Fig. 9** Histological studies with H&E staining (a) and Masson's trichrome staining (b) of skin tissues.

The wound healing process is highly correlated with cytokine-regulated cellular activities. Therefore, tumor necrosis factor-α (TNF-α) and vascular endothelial growth factor (VEGF) were chosen as indicators to evaluate the healing process of the CS/PEG/GOx@Co-MOF hydrogel. As shown in Fig. 10a, the expression of TNF-α on day 9 was significantly higher than that on day 22 for all five groups, and the expression level of the CS/PEG/GOx@Co-MOF hydrogel group was the lowest. These findings suggest that the dual antibacterial effect of the hydrogel promotes the transition of the wound from the inflammatory phase to the remodeling phase. VEGF immunostaining data show that the expression level

of the CS/PEG/GOx@Co-MOF hydrogel group was higher than that of other groups (Fig. 10b). In summary, the CS/PEG/GOx@Co-MOF hydrogel demonstrated better therapeutic effects during wound healing by down-regulating the expression of TNF-α and up-regulating the expression of VEGF.

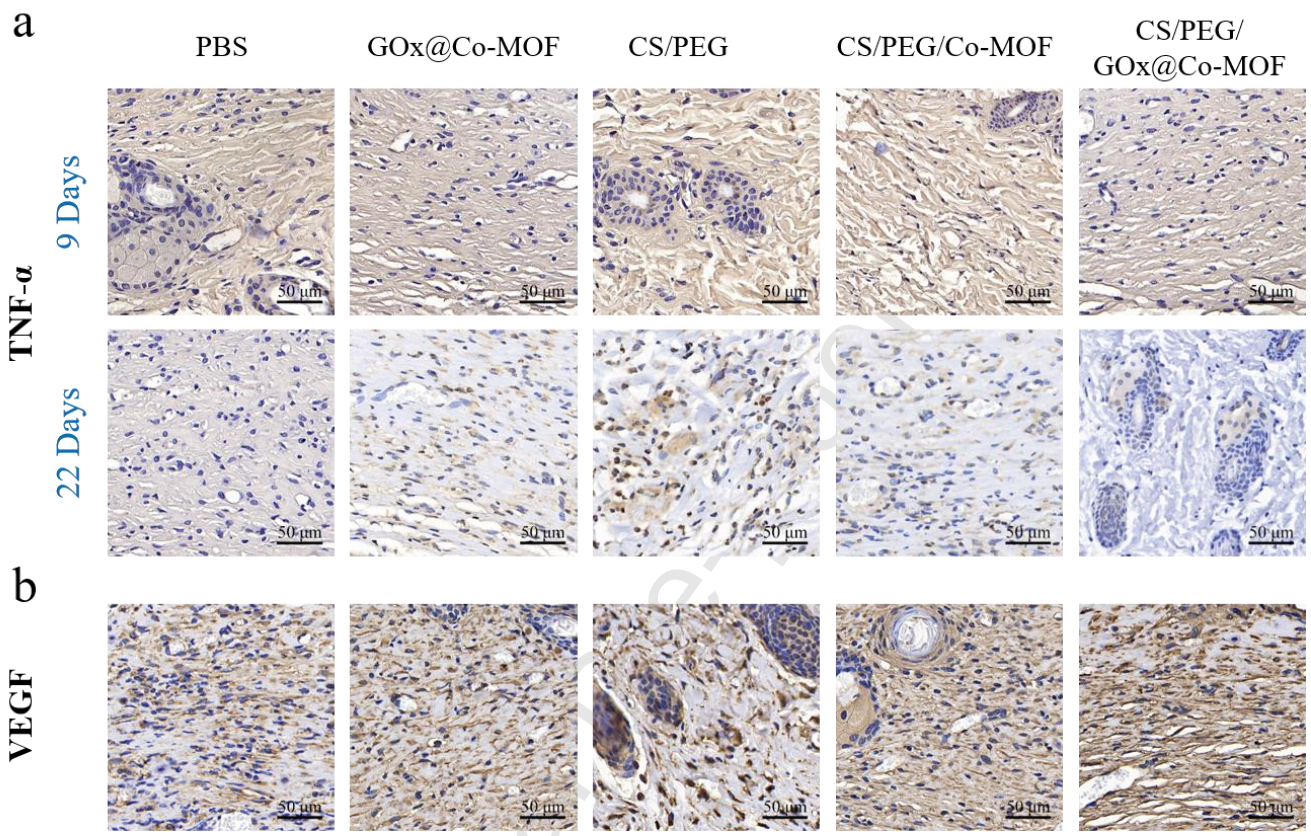


**Fig. 10** Immunohistochemical (IHC) staining of TNF-α after 9 and 22 days (a), and VEGF (b) of the five groups.

## 4. Conclusions

This work successfully developed a chitosan-based hydrogel dressing loaded with glucose oxidase/cobalt metal-organic frameworks (GOx@Co-MOF), exhibiting significant antibacterial and wound-healing capabilities. This composite hydrogel presents several advantages. First, Co-MOF effectively avoids the loss of GOx enzyme activity while ensuring high loading content. Second, the release of $H_2O_2$ and $Co^{2+}$ plays a dual antibacterial role and can achieve long-term antibacterial effect. Third, the good biocompatibility of chitosan-based hydrogels, combined with excellent self-healing properties, should allow potential applications in various types of wounds. The wound healing and in

vivo antibacterial results in mice show that CS/PEG/GOx@Co-MOF hydrogel can prevent bacterial infection and accelerate wound healing. In conclusion, the unique properties and effective performance in both antibacterial activity and wound healing of the CS/PEG/GOx@Co-MOF hydrogel highlight its potential for further development and clinical application as a new generation of wound dressing materials.

**Declaration of competing interest**

The authors have no conflicts of interest.

**Acknowledgments**

The work was financially supported by the Shandong Provincial Natural Science Foundation (grant N° ZR2021ME208, ZR2022ME083), Shandong Province Medical and Health Science and Technology Development Program (202104130109), and Qingdao Municipality Key Technology Research and Industrialization Demonstration Project.

## References

[1] R. Xu, G. Luo, H. Xia, W. He, J. Zhao, B. Liu, J. Tan, J. Zhou, D. Liu, Y. Wang, Z. Yao, R. Zhan, S. Yang, J. Wu, Novel bilayer wound dressing composed of silicone rubber with particular micropores enhanced wound re-epithelialization and contraction, Biomaterials 40 (2015) 1-11.

[2] R. Wang, J. Li, W. Chen, T. Xu, S. Yun, Z. Xu, Z. Xu, T. Sato, B. Chi, H. Xu, A Biomimetic Mussel-Inspired ε-Poly-l-lysine Hydrogel with Robust Tissue-Anchor and Anti-Infection Capacity, Adv. Funct. Mater. 27(8) (2017) 1604894.

[3] J. He, M. Shi, Y. Liang, B. Guo, Conductive adhesive self-healing nanocomposite hydrogel wound dressing for photothermal therapy of infected full-thickness skin wounds, Chem. Eng. J. 394 (2020) 124888.

[4] D. Simoes, S.P. Miguel, M.P. Ribeiro, P. Coutinho, A.G. Mendonca, I.J. Correia, Recent advances on antimicrobial wound dressing: A review, Eur. J. Pharm. Biopharm. 127 (2018) 130-141.

[5] S. Liu, X. Liu, Y. Ren, P. Wang, Y. Pu, R. Yang, X. Wang, X. Tan, Z. Ye, V. Maurizot, B. Chi, Mussel-Inspired Dual-Cross-linking Hyaluronic Acid/epsilon-Polylysine Hydrogel with Self-Healing and Antibacterial Properties for Wound Healing, ACS Appl. Mater. Interfaces 12(25) (2020) 27876-27888.

[6] D. Kong, Q. Zhang, J. You, Y. Cheng, C. Hong, Z. Chen, T. Jiang, T. Hao, Adhesion loss mechanism based on carboxymethyl cellulose-filled hydrocolloid dressings in physiological wounds environment, Carbohydr. Polym. 235 (2020) 115953.

[7] W. Li, Q. Yu, H. Yao, Y. Zhu, P.D. Topham, K. Yue, L. Ren, L. Wang, Superhydrophobic hierarchical fiber/bead composite membranes for efficient treatment of burns, Acta Biomater. 92 (2019) 60-70.

[8] A. Memic, T. Abudula, H.S. Mohammed, K. Joshi Navare, T. Colombani, S.A. Bencherif, Latest Progress in Electrospun

Nanofibers for Wound Healing Applications, ACS Appl. Bio Mater. 2(3) (2019) 952-969.
[9] X. Zhao, H. Wu, B. Guo, R. Dong, Y. Qiu, P.X. Ma, Antibacterial anti-oxidant electroactive injectable hydrogel as self-healing wound dressing with hemostasis and adhesiveness for cutaneous wound healing, Biomaterials 122 (2017) 34-47.
[10] Y. Li, J. Wang, Y. Wang, W. Cui, Advanced electrospun hydrogel fibers for wound healing, Compos. B. Eng. 223 (2021).
[11] G. Sun, Y.I. Shen, J.W. Harmon, Engineering Pro-Regenerative Hydrogels for Scarless Wound Healing, Adv. Healthc. Mater. 7(14) (2018) e1800016.
[12] Y. Yao, A. Zhang, C. Yuan, X. Chen, Y. Liu, Recent trends on burn wound care: hydrogel dressings and scaffolds, Biomater. Sci. 9(13) (2021) 4523-4540.
[13] F. Wu, G. Meng, J. He, Y. Wu, F. Wu, Z. Gu, Antibiotic-loaded chitosan hydrogel with superior dual functions: antibacterial efficacy and osteoblastic cell responses, ACS Appl. Mater. Interfaces 6(13) (2014) 10005-10013.
[14] H. Samadian, H. Maleki, Z. Allahyari, M. Jaymand, Natural polymers-based light-induced hydrogels: Promising biomaterials for biomedical applications, Coord. Chem. Rev. 420 (2020) 213432.
[15] S.A. Varghese, S.M. Rangappa, S. Siengchin, J. Parameswaranpillai, Natural polymers and the hydrogels prepared from them, Hydrogels Based on Natural Polymers2020, pp. 17-47.
[16] K. Ravishankar, R. Dhamodharan, Advances in chitosan-based hydrogels: Evolution from covalently crosslinked systems to ionotropically crosslinked superabsorbents, React. Funct. Polym. 149 (2020) 104517.
[17] J. Song, C. Zhang, S. Kong, F. Liu, W. Hu, F. Su, S. Li, Novel chitosan based metal-organic polyhedrons/enzyme hybrid hydrogel with antibacterial activity to promote wound healing, Carbohydr. Polym. 291 (2022) 119522.
[18] Y. Xie, X. Liao, J. Zhang, F. Yang, Z. Fan, Novel chitosan hydrogels reinforced by silver nanoparticles with ultrahigh mechanical and high antibacterial properties for accelerating wound healing, Int. J. Biol. Macromol. 119 (2018) 402-412.
[19] X. Zhao, M. Zheng, X. Gao, J. Zhang, E. Wang, Z. Gao, The application of MOFs-based materials for antibacterials adsorption, Coord. Chem. Rev. 440 (2021) 213970.
[20] F. Akbarzadeh, M. Motaghi, N.P.S. Chauhan, G. Sargazi, A novel synthesis of new antibacterial nanostructures based on Zn-MOF compound: design, characterization and a high performance application, Heliyon 6(1) (2020) e03231.
[21] S. Mallakpour, E. Nikkhoo, C.M. Hussain, Application of MOF materials as drug delivery systems for cancer therapy and dermal treatment, Coord. Chem. Rev. 451 (2022) 214262.
[22] A. Yuan, Y. Lu, X. Zhang, Q. Chen, Y. Huang, Two-dimensional iron MOF nanosheet as a highly efficient nanozyme for glucose biosensing, J. Mater. Chem. B 8(40) (2020) 9295-9303.
[23] J.H. Jo, H.C. Kim, S. Huh, Y. Kim, D.N. Lee, Antibacterial activities of Cu-MOFs containing glutarates and bipyridyl ligands, Dalton Trans. 48(23) (2019) 8084-8093.
[24] J. Liu, J. Liang, J. Xue, K. Liang, Metal-Organic Frameworks as a Versatile Materials Platform for Unlocking New Potentials in Biocatalysis, Small 17(32) (2021) e2100300.
[25] C. Guo, F. Cheng, G. Liang, S. Zhang, Q. Jia, L. He, S. Duan, Y. Fu, Z. Zhang, M. Du, Copper-based polymer-metal–organic framework embedded with Ag nanoparticles: Long-acting and intelligent antibacterial activity and accelerated wound healing, Chem. Eng. J. 435 (2022) 134915.
[26] Y. Yu, G. Chen, J. Guo, Y. Liu, J. Ren, T. Kong, Y. Zhao, Vitamin metal–organic framework-laden microfibers from microfluidics for wound healing, Mater. Horizons 5(6) (2018) 1137-1142.
[27] X. Fang, Y. Liu, M. Zhang, S. Zhou, P. Cui, H. Hu, P. Jiang, C. Wang, L. Qiu, J. Wang, Glucose oxidase loaded thermosensitive hydrogel as an antibacterial wound dressing, J. Drug Delivery Sci. Technol. 76 (2022) 103791.
[28] R. Singh, A. Sharma, J. Saji, A. Umapathi, S. Kumar, H.K. Daima, Smart nanomaterials for cancer diagnosis and treatment, Nano Converg. 9(1) (2022) 21.
[29] Y. Du, X. Jia, L. Zhong, Y. Jiao, Z. Zhang, Z. Wang, Y. Feng, M. Bilal, J. Cui, S. Jia, Metal-organic frameworks with different dimensionalities: An ideal host platform for enzyme@MOF composites, Coord. Chem. Rev. 454 (2022) 214327.
[30] H. An, J. Song, T. Wang, N. Xiao, Z. Zhang, P. Cheng, S. Ma, H. Huang, Y. Chen, Metal-Organic Framework

Disintegrants: Enzyme Preparation Platforms with Boosted Activity, Angew. Chem. Int. Ed. 59(38) (2020) 16764-16769.

[31] Y. Zhang, L. Tao, S. Li, Y. Wei, Synthesis of multiresponsive and dynamic chitosan-based hydrogels for controlled release of bioactive molecules, Biomacromolecules 12(8) (2011) 2894-2901.

[32] R. Re, N. Pellegrini, A. Proteggente, A. Pannala, M. Yang, C. Rice-Evans, Antioxidant activity applying an improved ABTS radical cation decolorization assay, Free Radic. Biol. Med. 26(9-10) (1999) 1231-1237.

[33] S. Zhao, L. Li, H. Wang, Y. Zhang, X. Cheng, N. Zhou, M.N. Rahaman, Z. Liu, W. Huang, C. Zhang, Wound dressings composed of copper-doped borate bioactive glass microfibers stimulate angiogenesis and heal full-thickness skin defects in a rodent model, Biomaterials 53 (2015) 379-391.

[34] L. Zhang, Z. Liu, Q. Deng, Y. Sang, K. Dong, J. Ren, X. Qu, Nature-Inspired Construction of MOF@COF Nanozyme with Active Sites in Tailored Microenvironment and Pseudopodia-Like Surface for Enhanced Bacterial Inhibition, Angew. Chem. Int. Ed. 60(7) (2021) 3469-3474.

[35] S.M. Ramish, A. Ghorbani-Choghamarani, M. Mohammadi, Microporous hierarchically Zn-MOF as an efficient catalyst for the Hantzsch synthesis of polyhydroquinolines, Sci. Rep. 12(1) (2022) 1479.

[36] Y. Su, Z. Li, H. Zhou, S. Kang, Y. Zhang, C. Yu, G. Wang, Ni/carbon aerogels derived from water induced self-assembly of Ni-MOF for adsorption and catalytic conversion of oily wastewater, Chem. Eng. J. 402 (2020) 126205.

[37] W. Zhou, L. Gao, Y. Zhang, T. Hu, Composites of Ni-MOF and polyaniline hydrogel for carbon monoxide resistant excellent catalysts of ethanol oxidation reaction, Int. J. Hydrog. 46(53) (2021) 27128-27137.

[38] H. Luo, H. Peng, Q. Zhao, High flux $Mg^{2+}/Li^{+}$ nanofiltration membranes prepared by surface modification of polyethylenimine thin film composite membranes, Appl. Surf. Sci. 579 (2022) 152161.

[39] Y. Li, M. Xie, X. Zhang, Q. Liu, D. Lin, C. Xu, F. Xie, X. Sun, Co-MOF nanosheet array: A high-performance electrochemical sensor for non-enzymatic glucose detection, Sens. Actuators B Chem. 278 (2019) 126-132.

[40] Y.-P. Zhu, Y.-P. Liu, T.-Z. Ren, Z.-Y. Yuan, Self-Supported Cobalt Phosphide Mesoporous Nanorod Arrays: A Flexible and Bifunctional Electrode for Highly Active Electrocatalytic Water Reduction and Oxidation, Adv. Funct. Mater. 25(47) (2015) 7337-7347.

[41] S.S. Nadar, V.K. Rathod, One pot synthesis of α-amylase metal organic framework (MOF)-sponge via dip-coating technique, J. Biol. Macromol. 138 (2019) 1035-1043.

[42] E. Mele, Electrospinning of natural polymers for advanced wound care: towards responsive and adaptive dressings, J. Mater. Chem. B 4(28) (2016) 4801-4812.

[43] C. Zhang, X. Wang, M. Hou, X. Li, X. Wu, J. Ge, Immobilization on Metal-Organic Framework Engenders High Sensitivity for Enzymatic Electrochemical Detection, ACS Appl. Mater. Interfaces 9(16) (2017) 13831-13836.

[44] J. Liu, D. Wu, N. Zhu, Y. Wu, G. Li, Antibacterial mechanisms and applications of metal-organic frameworks and their derived nanomaterials, Trends Food Sci. Technol. 109 (2021) 413-434.

[45] D. Li, T. Chen, Y. Zhang, Y. Xu, H. Niu, Synergistical Starvation and Chemo-Dynamic Therapy for Combating Multidrug-Resistant Bacteria and Accelerating Diabetic Wound Healing, Adv. Healthc. Mater. 10(18) (2021) e2100716.

[46] X. Zhao, B. Guo, H. Wu, Y. Liang, P.X. Ma, Injectable antibacterial conductive nanocomposite cryogels with rapid shape recovery for noncompressible hemorrhage and wound healing, Nat. Commun. 9(1) (2018) 2784.